Strain Dependent Structural Changes of Spider Dragline Silk

Anja Glišović,† Thorsten Vehoff,† Richard J. Davies,‡ and Tim Salditt*,†

Institut für Röntgenphysik, Georg-August-Universität Göttingen, Friedrich-Hund-Platz 1, 37077 Göttingen, Germany, and 2 ESRF, 6 Rue Jules Horowitz, BP220, 38043 Grenoble Cedex, France

Received March 2, 2007; Revised Manuscript Received November 5, 2007

ABSTRACT: Spider dragline silk is a natural semicrystalline polymer that is well-known for its unusual combination of tensile strength and extensibility. However, the correlation between structure and mechanical properties is still largely unknown. We have investigated the changes of the fiber's structure as probed by single fiber X-ray diffraction using a microfocus synchrotron beam, under controlled simultaneous mechanical load and variation of the humidity. Crystallite orientation, size, and lattice constants have been monitored while pulling the fibers.

1. Introduction

Spider silk is a biomaterial with fascinating mechanical properties.[1,2] Dragline silk can support relatively large strains and has a tensile strength comparable to steel or Kevlar. It is a material of high tenacity (toughness): values of 160 MJ/m^3 have been reported.[3,4] The dragline is produced in the spider's major ampullate gland and is one specific fiber out of seven different silk types which a *Nephila* spider has at hand.[5] The orb web's radii and the web's frame are built from dragline fibers, which have typical diameters in the range of 1−10 μm, depending on the species. Dragline also acts as the spider's life line, catching the spider when she drops from her web in moments of danger. Correspondingly, it is optimized for tensile strength, extensibility, and energy dissipation. Energy dissipation prevents unwanted springlike elasticity in functions related to catching of prey and stopping the spider from a free fall. An understanding of the structural origins of these mechanical properties is not only of fundamental interest but also needed in view of promising biomimetic applications.[6,7] More generally, the correlation between structure and the mechanical properties is of great importance in biomaterials, where evolution has often accomplished outstanding performance by complex hierarchical structures and self-assembly on molecular and mesoscopic length scales. Today, advanced structural characterization and modeling has led to a quantitative understanding of many biomaterials like bone, tendons and wood.[8,9] Such efforts have also led to considerable progress in the structural characterization of spider silk. Notably, X-ray fiber diffraction[10] has been used to investigate the secondary structure and folding of the silk proteins (spidroins) making up the fiber. A composite structure could be deduced with β-sheet crystallites embedded in an amorphous matrix, as described in the next section. However, scattering experiments from single fibers with a typical diameter of 4−9 μm (dragline silk) are extremely challenging.[11−13] In seminal work, Riekel and Vollrath have shown[14−16] that diffraction pattern can be obtained not only on thick samples of fiber bundles, but also on a single fiber, using highly brilliant microfocused undulator radiation of a third-generation synchrotron radiation facility, such as the ESRF in Grenoble. Building upon these results, we have used single fiber diffraction for the first time under simultaneous controlled mechanical load in order to investigate changes of the molecular structure with increasing strain up to failure. Note that Becker, Kaplan, and co-workers have also previously measured the change in the lattice constant in the regime of linear elasticity, using large fiber bundles under a load.[1,17] However, single fiber diffraction, where possible, is much better suited to correlate the structure to a controlled mechanical load, since the strain distribution in bundles is intrinsically inhomogeneous, and the majority of load may be taken up by a small minority of fibers.

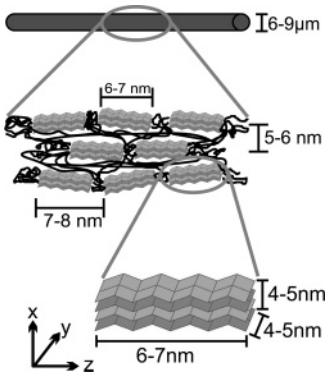

Figure 1. Schematic of spider dragline silk with the nanocrystallites embedded in the amorphous matrix (not drawn to scale). The scale bars indicate (from top to bottom) the diameter of the fiber, the length of the crystallite, the lateral spacing between adjacent crystallites, the vertical spacing between crystallites, the lateral lattice constants, and finally the vertical lattice constant.

2. Samples: Origin and Composition

The specific silk fibers which we address here are the dragline fibers of three *Nephila* species, namely, *N. clavipes* (NC), *N. madagascariensis* (NM), and *N. senegalensis* (NS). *Nephila* dragline consists of two proteins: *Spidroin I*[18] and *Spidroin II*.[19] Both sequences are characterized by repeated blocks of glycine and alanine rich motifs, leading to segments with alternating chemical functionality, somewhat similar to synthetic block copolymers.[20] While the shorter alanine blocks are associated with the crystalline fraction consisting of antiparallel β-sheet nanocrystallites, the glycine rich blocks are likely to form an amorphous matrix (volume fraction of presumingly 70−80%), in which the crystallites are embedded similar to synthetic semicrystalline polymers.[1,21−23] The β-sheet crystallites gives rise to broadened diffraction peaks while the amorphous matrix causes an isotropic scattering halo from which only a mean

* To whom correspondence should be addressed.
† Georg-August-Universität Göttingen.
‡ 2 ESRF.

10.1021/ma070528p CCC: $40.75
Published on Web 12/19/2007

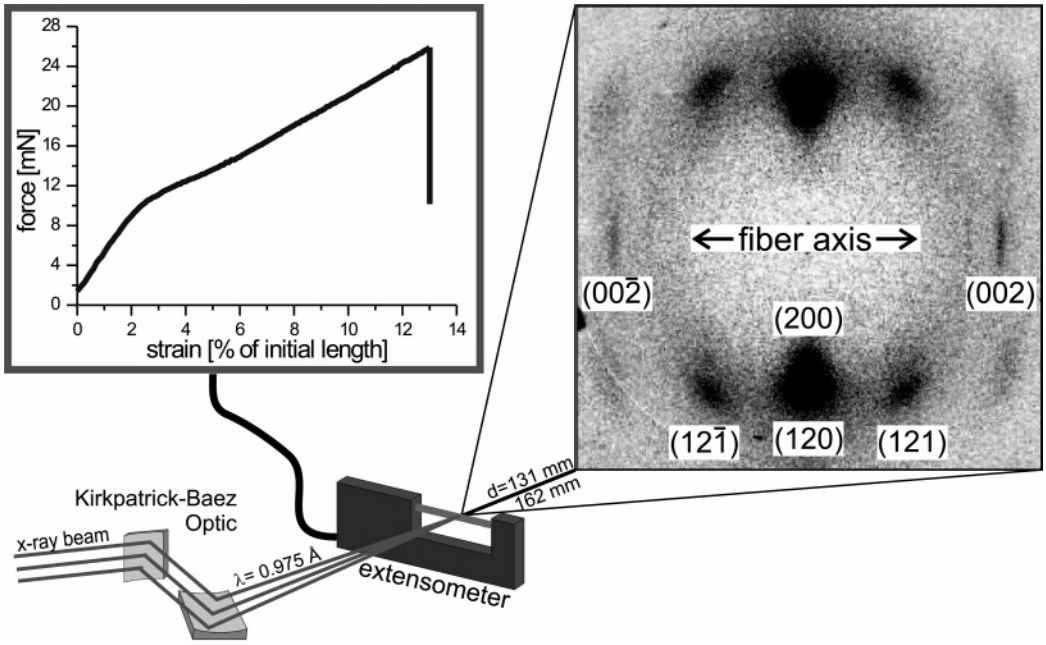

Figure 2. Schematic of the experimental setup at ID 13. The image in the upper right corner shows a diffraction pattern with the size-broadened reflections indexed to the orthorhombic lattice. The beam was focused with a Kirk−Patrick−Baez mirror system to a 7 μm spot at the sample. The CCD detector (Mar Research, Germany) was placed 131 mm behind the sample for NM and NC and for NS 161 mm. The extension of the fiber was paused during X-ray data accumulation to stabilize the fiber (5−6 μm) in the focal spot (7 μm).

distance of amino acid residues can be retrieved (≈3.26 Å). The β-sheets of all three *Nephila* species investigated can be classified to the Warwicker System 3.[24] Accordingly, these types of antiparallel β-pleated sheets have a nearly orthorhombic unit cell[25] with 10.6 Å × 9.44 Å × 6.95 Å.[24] To fix the coordinate system, we define the *x*-axis to be the axis in the direction of the amino acid side chains connecting different β-sheets with a lattice constant of $a = 10.6$ Å while the *y*-axis denotes the direction along the hydrogen bonds of the β-sheets with a lattice constant of $b = 9.44$ Å. Finally the *z*-axis corresponds to the axis along the covalent peptide bonds (main chain) with a lattice constant $c = 6.95$ Å. The short *c*-axis is well-aligned along the fiber axis, see Figure 1, while the *a*- and *b*-axis are randomly distributed around the fiber axis.[26,27] The size of the crystallites varies slightly for all three species. The mean values of all our measurements on *Nephila* draglines (single fiber and bundle[27]) corresponds to crystallites sizes of 53 Å × 47 Å × 60 Å ($a \times b \times c$), as determined from the Debye−Scherrer formula, in agreement with previous studies.[1] Note however, that the crystallites of *N. senegalensis* are somewhat larger than the crystallites of *N. madagscariensis* and *N. clavipes*. The single fibers were collected by a variation of forced silking.[28] The spiders were sedated in the refrigerator for 1 and $^1/_2$ hours at temperatures between 0 and 5 °C. Afterward the spiders were fixed upside down on a piece of styrofoam to expose the spinning apparatus. The sedation by cooling prevented that the spider got injured during the fixation. Once they were fully active again (but under inhibited mobility due to the fixation), the spinnerets were stimulated with a brush and the dragline threads were selected from other silk fibers. Then the two dragline fibers, stemming from neighboring identical glands, were parted from each other and reeled up separately.

3. Experiment

In order to study changes of the molecular structure with external strain up to breaking we have combined single fiber X-ray diffraction experiments with in situ force−strain measurements. The fibers were mounted in a high-resolution extensometer (LEX 810, Dia-Stron Ltd., Andover, Hampshire, U.K.). The length of the fibers was 30 mm to provide sufficient space for alignment. The stretching device consisted of an optically encoded micrometer drive and a piezo load cell with a maximum load of 2500 mN and force resolution of 0.05 mN. The experiments have been carried out at the microfocus beamline ID13 at ESRF, Grenoble.[29] A 12.7 keV X-ray beam was focused with a pair of short focal length Kirkpatrick Baez (KB) mirrors[30] to a 7 μm spot at the sample. This focusing scheme provides a sufficient flux density (6.8×10^{15} cps/mm^2) to obtain diffraction patterns from single dragline fibers but also increases the risk of radiation damage. To prevent artifacts from radiation damage, we have performed the experiment in the following way: (i) elongation of the sample to a preset strain, (ii) keeping the sample at this strain, (iii) taking one 1 s exposure, (iv) translation of the sample by 20 μm to the left along the horizonally positioned fiber, (v) realignment of the sample in the beam, (vi) repeating steps iii to iv 10 times to 11 1 s at the preset strain value, and (vii) finally reiteration of steps i−vi at the next higher strain value. Note that the sample was not exposed to the beam for the entire time, but only a vanishing fraction of the strain pause was actually used for data collection. Most of the time was spent on scanning the motors and readjustment procedures, since the fiber moved slightly when stretched. During motor movement, data readout, and keyboard input, the sample was protected from the beam by a fast shutter in order to prevent beam damage. Typically, the strain-pauses lasted up to 5 min. During the pause, relaxation occurs in the fiber. The pauses were necessary to keep the fiber stable in the beam, which is essential, given the 7 μm spot and the 5 μm fiber. Therefore the force−strain curves exhibit a sawtooth pattern, see Figures 2 and 3. The relaxation of the fibers measured at ID 13 was compared to the relaxation behavior of nonirradiated fibers, and no difference was observed. These experiments were performed under ambient conditions at around 50% relative humidity (RH) and 23 °C.

3.1. Immersed Fibers. As a control, and to investigate the influence of hydration, a different set of experiments was performed in a second ID13 beamtime using a climate chamber at varied RH For this purpose, a chamber for the LEX 810 was designed with respect to the requirements of single fiber X-ray diffraction. This humidity chamber consists of a housing for the extensometer's entire sample area, welded from 2 mm steel plates, with two 80 mm ×

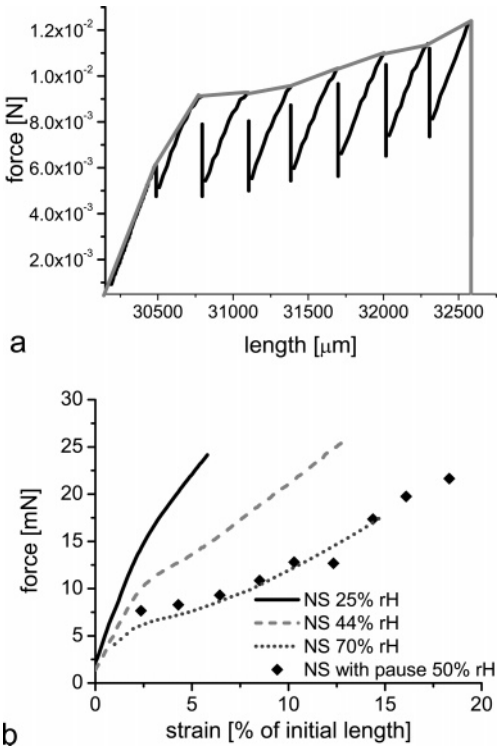

Figure 3. (a) Force−strain curve for a NM fiber. The initial length of the fiber was 30 mm. The cusps in the curve reflect the pauses during stretching, at which X-ray data accumulation took place. The envelope of the curve connecting the upper force values is equivalent to a force−strain curve without pauses and was used to calculate the energy necessary to stretch the fiber (area under the curve). (b) Force−strain curves measured at different relative humidities (lines). The break elongations appear shorter, because the curves are ensemble averages. The display of the curves was stopped as soon as the first rupture occurred. Data are shown for NS samples. The lines correspond to continuous measurements.[31] The ♦ indicate the force−strain values measured with pauses in the elongation at the microfocus X-ray experiment.

40 mm windows of 4 μm polypropylene foil serving as the beam pass. The chamber was connected to dry and humid nitrogen by 6 mm tubing. The humidity was set by mixing the nitrogen directly from the supply at less than 5% RH with a second reservoir which passed a water-filled gas-washing bottle with a maximum RH around 95%. The humidity was set my mixing the two streams, as controlled by a humidity and temperature sensor (Testo AG, Lenzkirch, Germany). For the second beamtime, the optics setup of the ID13 beamline had changed: the Kirkpatrick Baez (KB) mirrors[30] were replaced by compound refractive lenses which provided a significantly lower flux, as well as a larger spot of 10 μm at the sample, but with, however, a cleaner beam regarding beam profile and background. These changes caused an increase in the illumination time from 11 s to 60 s, in order to achieve diffraction patterns of similar signal-to-noise. Therefore a 60 s image was not split into a set of accumulations with shorter illumination time. Two types of experiments were performed: (1) The sample was placed in the extensiometer and equilibrated at humidities smaller than 5% RH (see Figure 5); after equilibration, it was extended to 0.5% of its initial length and a diffraction pattern was recorded. Then the sample was relaxed again, the humidity was increased to above 90%, and the sample was equilibrated at this humidity. The equilibration time in both cases was 30 min. Then a sequence of diffraction patterns should have been recorded starting again at 0.5% strain. However, this could not be accomplished because the construction of the extensiometer hindered the sample to fully contract when the humidity was increased. Because of this mounting, an internal stress occurred in the fibers which lead to failure after strain values bigger than 1%. (2) Therefore, we also performed a second type of experimental protocol, where the samples were first immersed in water, cut to the required size, and then placed in the extensiometer. In this configuration, a set of diffraction patterns at different strains was recorded at humidities above 90% RH, as described above, but in this case without internal strain from hindered supercontraction.

3.2. Raw Data Treatment. A typical single fiber diffraction pattern recorded with the CCD detector positioned 131 mm behind the sample (Mar 165 detector, Mar, Evanston, IL) at ambient conditions after data treatment is shown in Figure 2. One of the beamline's custom-made lead beamstops (approximately 300 μm diameter) was used to block the intense primary beam. The raw data were treated as follows: (i) both the image and the background (empty beam) were corrected by dark dark current and (ii) the (empty beam) background was subtracted from the image. The peaks which are significantly broadened by the small crystallite size (see below) can be indexed to the orthorombic lattice described above, see Figure 2.

4. Results

The two-dimensional (2D) intensity distribution was analyzed in the form of different one-dimensional (1D) cuts or slices. The lateral width of the 1D slices was optimized for signal-to-noise. At a pixel size of 157.88 μm corresponding to $\Delta q \simeq 7.2 \times 10^{-3}$ Å^{-1}, typically 11 one-pixel slices were summed up to generate a 1D slice. From the equatorial slices through the beam center and the equatorial peaks, the peak positions q_{120} and q_{200} of the two strongest peaks and their respective full width at half-maximum values (FWHM) were determined by least-square fitting, see Figure 4.

A detailed line shape analysis of the diffraction peaks indicates that Lorentzians are better suited to describe the tails of the peaks compared to Gaussian lineshapes.[26] We therefore chose the Lorentzian profiles for fitting the data although the modeling of crystalline reflections with Gaussians is more common. The feasibility of this choice will be discussed more extensively in the section about the amorphous halo.

The same procedure was applied to the (002)-peak in the meridional plane. As is well-known, the peak positions q_{hkl} give information about the lattice constants of the pseudo orthorhombic unit cell of the β-sheet crystallites,[24,25] while the FWHM is related to the crystallite size according to the Debye−Scherrer formula. Both the vertical slice through the (002)-peak as well as the off-axis slice through the (120)- and (121)-peaks contain information about the lattice parameter c. The intensity ratio of the (120)- and (200)-peaks varies between the three *Nephila* species, but the (200) intensity is always significantly smaller than (120). Therefore the fitting errors of the (200)-parameters are always considerably higher than those of (120).

Starting with the zero strain reference state, it was found that q_{120} and q_{200} values for all samples measured were somewhat smaller than the q-values expected from the work of Warwicker,[24] which is a classical reference for fiber proteins. However, the deviations are within the bounds of the Warwicker 3 class. Only for the species NM, the diffraction was intense enough to enable a full analysis of the (002)-peak and the q_{002} values obtained from this species are nearly in perfect agreement with literature. We now discuss the structural parameters and the associated changes of the diffraction pattern in the following sequence: (1) angular width of peaks reflecting the orientational distribution of the crystallites, (2) the radial width of the reflections indicative of the crystallite size, and finally (3) the position of the peaks reflecting the lattice constants. All parameters, including those which are not represented graphically, are tabulated in Tables 1 and 2. The error bars in the data shown in the figures indicate the standard error of mean = standard deviation/$\sqrt{n}$, were n is the number of independent measurements for each strain value ϵ. These errors of the

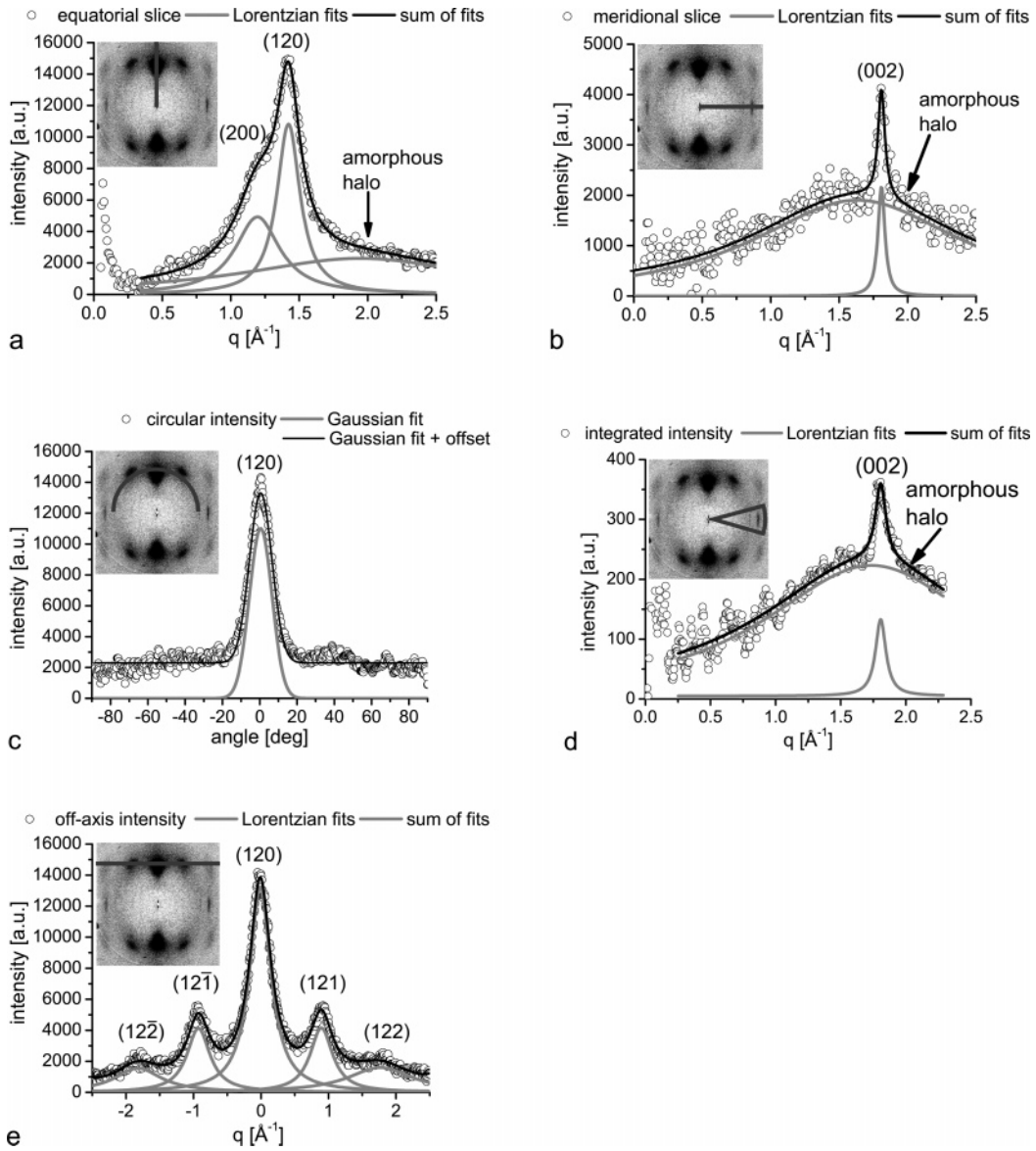

Figure 4. The intensities and fits along different slice and integration types used for analysis. For the angular intensity distribution a Gaussian curve was used. The other peaks were fitted by Lorentzians. (a) Equatorial slice through the main reflections (200) and (120). (b) Meridional slice through the (002)-reflection. (c) Circular slice through (120). (d) Integrated intensity showing the maxima of the amorphous halo and the (002)-reflection. (e) Off-axis slices through the (121)-peaks.

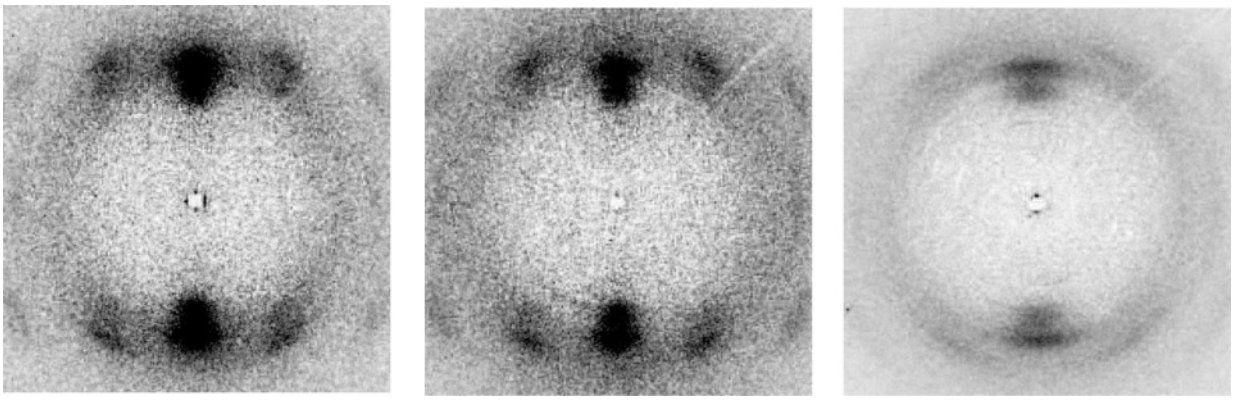

Figure 5. Comparison of diffraction patterns obtained from *N. madagascariensis*. Right: NM single fiber diffraction pattern at RH < 5%. Middle: NM single fiber diffraction pattern of the same fiber as in the right image but at RH > 90%. The increase of the humidity causes no visible changes in the diffraction patterns. Left: single fiber diffraction pattern of another NM fiber after immersion in water. The immersion causes a circular broadening of the reflections, see text.

individual data points have been fed in the linear regression and thereby determine the errors on the intercept and slopes tabulated in Tables 1 and 2.

4.1. Angular Width and Crystallite Orientation. From arc slices through the (120)-peak, an angular width aw_{120} of the intensity is obtained. This intensity distribution reflects the

Table 1. Linear Regression Results for NC and NM Crystallite Parameters for NC and NM; Values for NS Are Given in Table 2; Linear Regression Was Performed in an Interval of 1−8% Strain for NC and 0.5−8% Strain for NM; q_{hkl} Was Determined from Peak Position, Crystallite Size L_{hkl} from fwhm, Angular Width aw_{120} from Arc Slices as Shown in Figure 4c, *c*-Axis' Lattice Constant c_{002} from Meridional Slices as Shown in Figure 4b; c_{002}^{cake} from Cake Integration as Shown in Figure 4d; $c_{offaxis}$ from Slices as Shown in Figure 4e; The Linear Regime for d_{amorph} Starts at 2% Strain; The Correlation Coefficient is Denoted by "*R*"

	NC			NM		
x	intercept	slope	*R*	intercept	slope	*R*
q_{120}[Å]$^{-1}$	1.423	7.44×10^{-4}	0.78	1.423	-6.74×10^{-5}	−0.09
error	$\pm 9.99 \times 10^{-4}$	$\pm 2.44 \times 10^{-4}$		$\pm 4.35 \times 10^{-4}$	$\pm 1.34 \times 10^{-4}$	
q_{200}[Å]$^{-1}$	1.170	$-1.30E-4$	−0.05	1.185	-8.22×10^{-4}	−0.91
error	$\pm 2.85 \times 10^{-3}$	$\pm 6.44 \times 10^{-4}$		$\pm 1.04 \times 10^{-3}$	$\pm 2.70 \times 10^{-4}$	
q_{002}[Å]$^{-1}$				1.807	-1.21×10^{-3}	−0.83
error				$\pm 5.43 \times 10^{-4}$	$\pm 1.34 \times 10^{-4}$	
q_{cake}[Å]$^{-1}$				1.815	-1.17×10^{-3}	−0.76
error				$\pm 3.75 \times 10^{-4}$	$\pm 1.12 \times 10^{-4}$	
q_{halo}[Å]$^{-1}$				1.660	1.46×10^{-2}	0.99
error				$\pm 1.06 \times 10^{-2}$	$\pm 1.52 \times 10^{-3}$	
L_{120}[Å]	51.91	−0.60	−0.48	52.30	−0.81	−0.98
error	±1.48	±0.25		±0.60	±0.16	
L_{200}[Å]	52.98	−0.29	−0.41	49.12	0.23	0.68
error	±1.06	±0.26		±0.87	±0.16	
L_{002}[Å]				142.56	−4.28	−0.66
error				±4.97	±0.95	
L_{cake}[Å]				158.27	−3.48	−0.77
error				±4.29	±0.95	
aw_{120}[deg]	15.65	−0.40	−0.81	14.20	0.09	0.50
error	±0.56	±0.12		±0.43	±0.09	
c_{002}[Å]				6.952	4.76×10^{-3}	0.83
error				$\pm 2.10 \times 10^{-3}$	$\pm 5.26 \times 10^{-4}$	
c_{cake}[Å]				6.925	4.50×10^{-3}	0.76
error				$\pm 1.45 \times 10^{-3}$	$\pm 4.31 \times 10^{-4}$	
$c_{offaxis}$[Å]	6.902	8.75×10^{-3}	0.23	6.897	-1.71×10^{-5}	±0.00
error	$\pm 3.54 \times 10^{-2}$	$\pm 8.43 \times 10^{-3}$		$\pm 3.57 \times 10^{-3}$	$\pm 1.55 \times 10^{-3}$	
d_{amorph}[Å]				3.726	-1.91×10^{-2}	−0.80
error				$\pm 2.51 \times 10^{-2}$	$\pm 5.85 \times 10^{-3}$	
Δq_{amorph}[Å]$^{-1}$				1.817	-9.69×10^{-3}	−0.25
error				$\pm 6.19 \times 10^{-2}$	$\pm 1.29 \times 10^{-2}$	

distribution of the tilt angles ϕ of the local β-sheet *c*-axis with the fiber axis. The crystallites are always aligned with their longest side (*c*-axis) parallel to the direction of the fiber. From aw_{120}, an orientational order parameter $op = (3\cos(0.425aw)^2 - 1)/2$ can be defined.[1,27] $aw_{120}(\epsilon)$ is analyzed by a linear regression. Within the experimental errors, it is constant (NM, NS) or decreases (NC), see Figure 6 and Tables 1 and 2.

4.2. Radial Width and Crystallite Size. From the radial width of the reflection Δq_{hkl} (full width at half-maximum, FWHM) measured along radial slices (radial denotes slices extending through the origin, thus perpendicular to angular slices), the crystallite size L_{hkl} along the direction corresponding to the reflection can be calculated from the well-known Debye−Scherrer formula $L = k4\pi/\Delta q$. For the shape factor, a parameter value $k = 0.9$ was used, ranging in between the parameters derived for a sphere ($k = 0.89$) or a cube ($k = 0.94$). The three most prominent peaks (120), (200), and (002) were analyzed. The crystallite size along the *b*-axis (0*k*0) is calculated from the (120)-peak, along with the predetermined size from the (200)-peak. However, since the (200)-peak is only observed as a shoulder to the stronger (120)-peak, a clear separation of the lateral width along the *x* and *y* axes, respectively, is delicate and subject to significant errors. Note that the changes in lateral crystallite size cannot be explained by an affine deformation of the crystal at constant volume, since in this case the lattice constants (peak positions) would decrease in contrast to the observation. At zero or low strain, the crystallite size determined along the *x* and *y* axis, respectively, from the Debye−Scherrer formula for the three species were NS = 67 Å, 48 Å; NM = 50 Å, 46 Å; and NC = 43 Å, 48 Å. These values are in good agreement with previous measurements of fiber bundles. The value found for the crystallites length along the *c*-axis in the single fiber experiment was problematic, as discussed below.

First we consider $\Delta q_{120}(\epsilon)$, which behaves alike for all three *Nephila* species. While the peak positions q_{120} and q_{200} do not change with strain, $\Delta q_{120}(\epsilon)$ increases linearly, and the lateral crystallite size decreases correspondingly. Up to 8% strain, L_{120} decreases from 52 Å down to 46 Å corresponding to an average loss of 1.5 Bragg planes. We attribute this loss of more than one lattice plane to a strain induced unfolding or fracturing (splitting) of the β-sheet crystallites along the direction of the hydrogen-bonds. Next we consider the crystallite size L_{200} calculated from the (200)-reflection. This peak shows a different behavior for different species. There was no strain-dependency observable for NC and NM. For NS, L_{200} decreases from 66 Å down to 45 Å at 20% strain, corresponding to a decrease of two Bragg planes. However, as stated above, the results for the (200)-peak are always very susceptible to the details of the fitting approach (line shape, parameter initialization). The high covariance with the (120)-peak parameters make it difficult, if not impossible, to single out the (200)-peak parameters in a unique manner.

We now consider the crystallite's size along the *z*-axis. Unfortunately, only for NM, the (002)-reflection was pronounced enough to allow for a quantitative analysis. The width Δq_{002} of the (002)-reflection was obtained from meridional slices and cake integrations. Both methods yield consistent results. The corresponding length L_{002} shows no dependency on the strain, while the corresponding lattice constant q_{002} does, see below. The low signal-to-noise of this peak leads to significant errors. In absolute numbers, the crystal size L_{002} along *z* varies between 150 and 100 Å. Compared to previously published results on fiber bundles,[1] this range of sizes is up to a factor of 2 larger. In other words, the peak width is about two times broader in the fiber bundle than in single fiber measurements, for reasons which are unclear to us.

Table 2. Values from Linear Regression of Different Crystallite Parameters for NS and NM; The Values for NC Are Given in Table 1; q_{hkl} Peak Position and L_{hkl} Crystallite Length Calculated from fwhm; aw_{120} Angular Width from Arc Slices, Shown in Figure 4c; c_{002} *c*-Axis' Lattice Constant Calculated from Meridional Slices, Shown in Figure 4b; c_{002}^{cake} *c*-Axis' Lattice Constant Calculated from Cake Integration, Shown in Figure 4d; $c_{offaxis}$ *c*-Axis' Lattice Constant Calculated From Slices as Shown in Figure 4e; The Linear Regime of the Mean Distance d_{amorph} Starts at 2% Strain; The Cake Integration Was Only Performed for NM Due to Its Sufficient Intensity of the Amorphous Halo; The Correlation Coefficient is Denoted by "*R*"

	NS			NM		
x	intercept	slope	*R*	intercept	slope	*R*
q_{120}[Å]$^{-1}$	1.423	7.71×10^{-5}	0.33	1.423	-6.74×10^{-5}	−0.09
error	$\pm 9.02 \times 10^{-4}$	$\pm 5.25 \times 10^{-4}$		$\pm 4.35 \times 10^{-4}$	$\pm 1.34 \times 10^{-4}$	
q_{200}[Å]$^{-1}$	1.162	-2.22×10^{-4}	−0.99	1.185	-8.22×10^{-4}	−0.91
error	$\pm 2.65 \times 10^{-3}$	$\pm 2.22 \times 10^{-4}$		$\pm 1.04 \times 10^{-3}$	$\pm 2.70 \times 10^{-4}$	
q_{002}[Å]$^{-1}$				1.807	-1.21×10^{-3}	−0.83
error				$\pm 5.43 \times 10^{-4}$	$\pm 1.34 \times 10^{-4}$	
q_{cake}[Å]$^{-1}$				1.815	-1.17×10^{-3}	−0.76
error				$\pm 3.75 \times 10^{-4}$	$\pm 1.12 \times 10^{-4}$	
q_{halo}[Å]$^{-1}$				1.660	1.46×10^{-2}	0.99
error				$\pm 1.06 \times 10^{-2}$	$\pm 1.52 \times 10^{-3}$	
L_{120}[Å]	52.91	−0.59	−0.83	52.30	−0.81	−0.98
error	±0.67	±0.05		±0.60	±0.16	
L_{200}[Å]	60.01	−0.37	−0.46	49.12	0.23	0.68
error	±0.89	±0.07		±0.87	±0.16	
L_{002}[Å]		-		142.56	−4.28	−0.66
error				±4.97	±0.95	
L_{cake}[Å]		-		158.27	−3.48	−0.77
error				±4.29	±0.95	
aw_{120}[deg]	15.95	−0.13	−0.79	14.20	0.09	0.50
error	±0.30	±0.02		±0.43	±0.09	
c_{002}[Å]				6.952	4.76×10^{-3}	0.83
error				$\pm 2.10 \times 10^{-3}$	$\pm 5.26 \times 10^{-4}$	
c_{cake}[Å]				6.925	4.50×10^{-3}	0.76
error				$\pm 1.45 \times 10^{-3}$	$\pm 4.31 \times 10^{-4}$	
$c_{offaxis}$[Å]				6.897	-1.71×10^{-5}	±0.00
error				$\pm 3.57 \times 10^{-3}$	$\pm 1.55 \times 10^{-3}$	
d_{amorph}[Å]		-		3.726	-1.91×10^{-2}	−0.80
error				$\pm 2.51 \times 10^{-2}$	$\pm 5.85 \times 10^{-3}$	
Δq_{amorph}[Å]$^{-1}$		-		1.817	-9.69×10^{-3}	−0.25
error				$\pm 6.19 \times 10^{-2}$	$\pm 1.29 \times 10^{-2}$	

Table 3. Crystal Parameters at Low Strains $\epsilon \leq 1\%$ and Different Humidities Obtained from *N. madagascariensis* Dragline

parameter	≤5% RH	≥90% RH	immersed
q_{120}[Å^{-1}]	$1.426 \pm (1.71 \times 10^{-3})$	$1.422 \pm (1.23 \times 10^{-3})$	$1.423 \pm (3.70 \times 10^{-3})$
q_{200}[Å^{-1}]	$1.168 \pm (1.02 \times 10^{-3})$	$1.171 \pm (3.55 \times 10^{-3})$	$1.178 \pm (4.20 \times 10^{-3})$
L_{120}[Å]	53.55 ± 1.38	58.68 ± 1.35	43.22 ± 3.53
L_{200}[Å]	39.79 ± 1.22	42.76 ± 1.98	47.15 ± 2.22
aw_{120}[deg]	$16.00 \pm (1.17 \times 10^{-1})$	$14.18 \pm (1.02 \times 10^{-1})$	$31.16 \pm (8.89 \times 10^{-1})$

4.3. Peak Position and Lattice Constants. The peak positions q_{120} and q_{200} were found to be independent or at most very weakly dependent on strain, when comparing the error of the slope with the modulus of the slope. Thus the lattice constants perpendicular to the direction of the force exhibit no or only a small strain dependence, see also Tables 1 and 2. Of all *q*-values, q_{002} showed the clearest correlation with strain. However, only for NM, this peak was sufficiently intense for analysis. With increasing strain, the lattice constant *c* increases for NM. Up to 9% strain, there is a nearly linear correlation with a 15:1 ratio. When the fiber is stretched by 5% of it is initial length, the lattice constant *c* increases by approximately 0.33%, see the linear fit in Figure 7a and the corresponding slope, see Tables 1 and 2. The off-axis slices support this observation only up to 4%. Above 4% strain, the values of the off-axis slices through the (121)-reflection are quite scattered. Furthermore, in absolute numbers, the lattice constant calculated from the off-axis slices is smaller than the value obtained from q_{002}, namely, $c_{off-axis} = 6.89$ Å compared to $c_{002} = 6.952$ Å. This shift seems to be intrinsic to the diffraction pattern and may possibly be explained by strain fields or defects. As can be seen for example in Figure 2, the (122)-peak is also shifted to higher *q*-values with respect to the (002)-peak.

4.4. Amorphous Halo. In samples of high-intensity it is also possible to analyze the scattering contribution of the amorphous matrix, i.e., the disordered polypeptide chains in which the crystallites are embedded and by which they are linked. As for the (002)-reflections, only NM samples showed a signal-to-noise ratios high enough for analysis. The amorphous halo can be analyzed best in the meridional plane where it is not overlapped by scattering from the crystalline fraction as can be seen by comparing Figure 4a and 4b. The peak center corresponds to the mean distance $d_{amorph} = 2\pi/q_{halo}$ of scatterers in the amorphous matrix, and exhibits a linear strain dependency. Starting with a value of $d_{amorph} = 3.72$ Å at $\epsilon = 2$ %, it decreases to approximately $d_{amorph} = 3.5$ Å at $\epsilon = 9\%$, see also Figure 7b. The width of the amorphous halo Δq_{amorph} exhibits no dependency on ϵ, see Tables 1 and 2. Note that the decrease in the mean distance parallel to the applied strain is difficult to interpret and is in contrast to the behavior of the lattice constant *c*. At the moment we do not have a satisfying explanation for this finding. Finally, let us briefly address the validity of the least-square analysis and the fitting model. A detailed line shape analysis of the diffraction peaks, has been carried out and is described in ref 26. The analysis indicates that Lorentzians are better suited to describe the tails of the peaks compared to

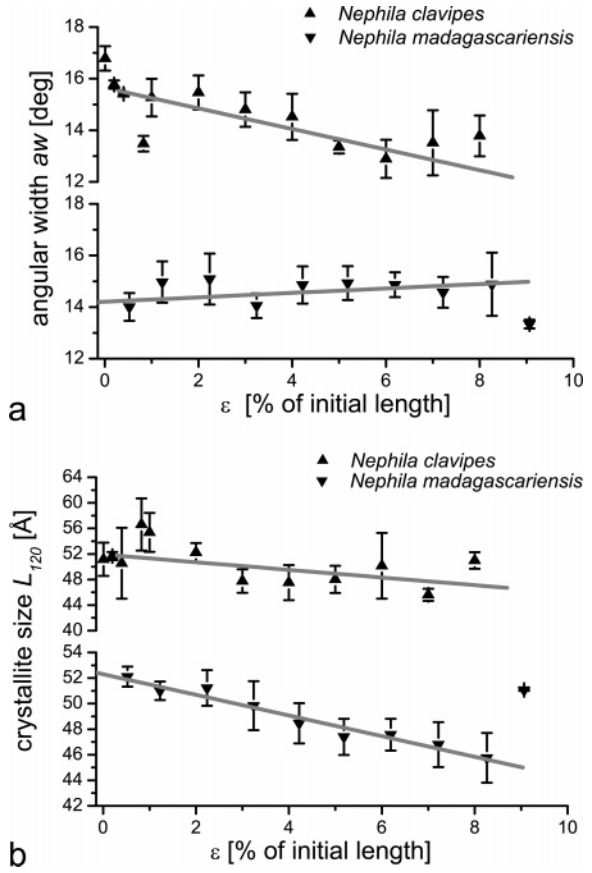

Figure 6. (a) Angular width aw of NM and NC samples versus strain. For NC, the decrease in aw indicates a significient increase in crystallite orientation, while a constant relationship is observed for NC. (b) Crystallite size L_{120} as a function of strain ϵ calculated from the width of the (120)-peak. The data show that the crystallite size perpendicular to the direction of the strain decreases.

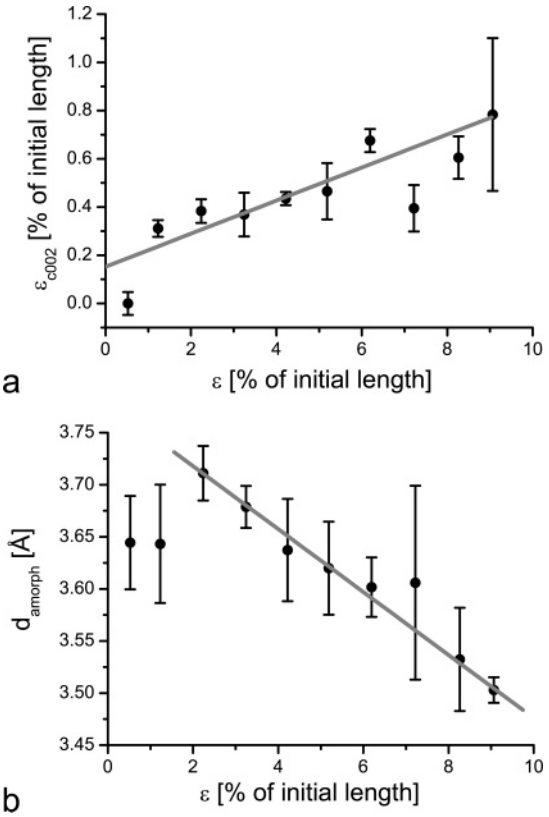

Figure 7. (a) The strain lattice ϵ_{c002} calculated from the relative changes of the lattice constant *c*, as obtained from the (002)-peak (shown for NM), as a function of external strain ϵ. (b) Analysis of the amorphous halo originating from the disordered chains. The mean distance of the amorphous matrix *a* parallel to the fiber axis decreases from 2% strain on.

Gaussian lineshapes. For example, for a typical NM curve, the least-square fitting yielded $\chi^2 = 1.21$ for the double Lorentzian and $\chi^2 = 5.17$ for the double Gaussian model.[26] We therefore chose the Lorentzian profiles for fitting the data although the modeling of crystalline reflections with Gaussians is more common. Importantly, the results on the peak position indicates that the mean deviation between the two models is small; for example, for the (120)-reflection, the relative error is smaller than 1% for the peak position and smaller than 10% for the crystallite size. A further source of systematic errors may be due to the amorphous halo in the equatorial cut which presents a broad background to the (200)- and (120)-reflections and influences the fitting results. Conversely, the peak position of the halo determined in that direction may not be very meaningful or conclusive since it is dominated by the stronger peaks. Note, however, that the change in the position of the amorphous halo is not strong enough to affect the broadening of the reflections, let alone to explain the observation of a peak broadening with strain.

5. Influence of Humidity and Strain

In Figure 5, the diffraction patterns of NM dragline at different humidities are shown. The two patterns have been taken at different relative humidities from the same fiber, after initial mounting and equilibration at RH < 5% and RH > 90%. The pattern of the immersed fiber is taken from another sample of the same species. The higher humidity induces only minor changes in the diffraction pattern while immersion in water causes a circular smearing of the reflections. Out of the ensemble of 26 NM and 4 NC fibers, only 3 series for NM provided high enough signal to measure the structures at low strain at both high and low humidities. Only one fiber survived a further elongation to 2% strain after increasing the humidity. So no systematic study of strain induced structural changes at high humidities was possible. Only the changes at low strain caused by increasing humidity could be investigated. The reason for breakage was obviously that mounting in the extensiometer while changing conditions from low to high humidity hindered the sample to fully contract when the humidity was increased. Because of this mounting, an internal stress builds up in the fibers which leads to breakage. This explanation is supported by the angular width of the reflections at different humidities. The observed angular width was 16 and 14 for humidities smaller than 5% RH and above 90% RH, respectively, see Table 3. The decrease of the angular width with increasing humidity of a fiber mounted first under low humidity is in sharp contrast

Table 4. Crystal Parameters of NM Dragline Obtained from Linear Regressions and Direct Measurements, Values with an Asterisk Are Mean Values Measured at Low Strains $\epsilon \leq 1\%$, Parameters without an Asterisk Are Obtained from the Parameters' Strain Dependency by Linear Regressions

parameter	NM ambient	NM immersed
L_{120}[Å]	52.30 ± 0.60	49.39 ± 2.51
L_{200}[Å]	49.12 ± 0.87	43.06 ± 0.59
aw_{120}[deg]	14.20 ± 0.43	26.94 ± 0.03
parameter	NM ≤5% RH	NM immersed
L^*_{120}[Å]	53.55 ± 1.38	43.22 ± 3.53
L^*_{200}[Å]	39.79 ± 1.22	47.15 ± 2.22
aw^*_{120}[deg]	16.00 ± 0.12	31.16 ± 0.89

Table 5. Linear Regression of Different Crystallite Parameters from Immersed Fibers; Linear Regression Was Performed in an Interval of 0.5−28% Strain for NM and 1−34% Strain for NC; q_{hkl} Was Obtained from the Peak Position, and the Crystallite Size L_{hkl} Calculated from the Width of the Corresponding Reaction; As Above, aw_{120} Was Obtained from the Arc Slices, as Shown in Figure 4c; The Correlation Coeffcient is Denoted by *"R"*

	NC			NM		
x	intercept	slope	*R*	intercept	slope	*R*
q_{120}[Å]$^{-1}$	1.426	-6.74×10^{-5}	−0.14	1.426	-1.03×10^{-4}	−0.36
error	$\pm 1.40 \times 10^{-3}$	$\pm 1.08 \times 10^{-4}$		$\pm 1.30 \times 10^{-3}$	$\pm 1.48 \times 10^{-4}$	
q_{200}[Å]$^{-1}$	1.183	-1.02×10^{-4}	−0.35	1.176	-2.54×10^{-4}	−0.57
error	$\pm 1.84 \times 10^{-3}$	$\pm 1.78 \times 10^{-4}$		$\pm 3.74 \times 10^{-3}$	$\pm 2.30 \times 10^{-4}$	
L_{120}[Å]	56.34	−0.48	−0.81	49.39	−0.09	−0.17
error	±1.61	±0.07		±2.51	±0.19	
L_{200}[Å]	44.34	0.27	0.46	43.06	0.07	0.48
error	±2.06	±0.11		±0.59	±0.05	
aw_{120}[Å]	26.48	−0.08	−0.98	26.94	1.30×10^{-3}	0.01
error	±0.56	±0.03		±0.03	±0.04	
d_{amorph}[Å]	3.873	$-9.23E-3$	−0.99	3.843	-3.87×10^{-3}	−0.71
error	$\pm 8.40 \times 10^{-3}$	$\pm 9.16 \times 10^{-4}$		$\pm 1.47 \times 10^{-2}$	$\pm 1.74 \times 10^{-3}$	
Δq_{amorph}[Å]	1.475	-8.17×10^{-3}	−0.79	1.624	-1.15×10^{-3}	−0.14
error	$\pm 7.78 \times 10^{-2}$	$\pm 3.80 \times 10^{-3}$		$\pm 1.19 \times 10^{-2}$	$\pm 2.64 \times 10^{-3}$	

with the nearly doubled angular width after immersion in water.

5.1. Immersed Fibers. Similar to the experiments at ambient conditions, the strain induced structural changes of immersed fibers have been investigated, see Tables 4 and 5. Because of the circular smearing of the reflections, the (002)-peak was not intense enough for analysis and only the (120)- and (200)-peaks were exploitable. Let us briefly address the main results.

5.1.1. Angular Width and Crystallite Orientation. From arc slices through the (120)-peak, the angular width aw_{120} is obtained. The order of the crystallites is decreased after immersion as evidenced by the higher angular width of approximately 27 compared to 14 in the dry state, see Table 4. The angular width $aw_{120}(\epsilon)$ was analyzed by a linear regression. Within the experimental errors, it is constant for NM but decreases for NC by approximately 3 down to 23.5 at $\epsilon = 34\%$, see Table 5.

5.1.2. Radial Width and Crystallite Size. From the FWHM (radial width) measured along the equatorial slice, the crystallite sizes L_{120} and L_{200} were calculated by the Debye−Scherrer formula. At zero or low strain, the crystallite size determined for the two species were NM = 43 Å × 43 Å × −Å and NC= 44 Å × 49 Å × −Å. Up to 28% strain, L_{120} for NM decreases from 59 Å down to 44 Å, corresponding to an average loss of 3.5 Bragg planes, and for NC, L_{120} decreases from 49 Å down to 37 Å, corresponding to an average loss of 3 Bragg planes.

5.1.3. Peak Position and Lattice Constants. The peak positions q_{120} and q_{200} were found to be independent of the applied strain within experimental errors, see also Table 5.

5.1.4. Amorphous Halo. The higher disorder of immersed dragline has the effect that the meridional (002)-reflection does no longer overlay the amorphous halo, see Figure 4. Therefore the amorphous halo was analyzed in the meridional slices and no cake integration was necessary. The amorphous peak center corresponds to the mean distance $d_{amorph} = 2\pi/q_{halo}$ of the scatterers in the amorphous matrix and exhibits a linear strain dependency. Starting with a value of $d_{amorph} = 3.87$ Å at $\epsilon = 1$ %, it decreases to approximately $d_{amorph} = 3.55$ Å at $\epsilon = 34\%$. The results for the immersed fibers are tabulated in Tables 3−5 and discussed in more detail in ref 33.

6. Summary and Discussion

With these single fiber experiments, we have shown that it is possible to observe mechanically induced structural changes in single dragline fibers by synchrotron X-ray scattering. It was found that the orientation of the β-sheet crystallites along the fiber axis, as well as the lattice constant *c* parallel to the strain direction, increases with increasing strain. At the same time, the radial width of the reflections along the equatorial axes is found to increase. Since it is unlikely that a strain effect would induce a broadening along the equatorial axes (*x*,*y*) but not in the meridional axis (*z*), we attribute this broadening to a decrease of the crystallite lateral size.

This pronounced decrease of the crystallite size can be interpreted by a partial splitting of the crystallites along the noncovalent bonds or a partial unfolding of chains at the interface to the amorphous matrix. This could happen if the polypeptide chains folding into the crystallite are excerting a shear force. The "splitting energy" needed to break the corresponding hydrogen and van der Waals bonds can be estimated to be of the same order as the total energy necessary for stretching the fiber. From the force−strain curves, e.g., such as shown in Figure 3a, we obtain a typical stretching energy of around 3.4×10^{-2} mJ for a single NM dragline fiber of 30 mm length, when stretched up to 8%. To compare this value to the splitting energy, the number of crystallites in the fiber as well as the mean splitting energy per crystallite have to be estimated. The experimental results indicate that the crystallite decreases by roughly 80 unit cells corresponding to about 1280 broken bonds. With these values and a crystalline fraction of 20%, the energy dissipated in a 30 mm fiber with 6 μm diameter is 4.6×10^{-2} mJ which is in the same energy range as the total energy for stretching. From hysteresis experiments,[31] we know that only 68% of the stretching energy is actually dissipated by irreversible processes (such as the breaking of bonds). So, while in the same energy range as the experimental values, the calculation of the dissipated energy by the simplistic estimation of bond energy can be regarded as an upper limit.

This rough estimate shows that splitting of the crystallites or better to an exfoliating of β-sheets at the internal surface of the crystalline and the amorphous regions is a plausible mechanism for energy dissipation. Possibly this exfoliation effect results from shear induced by mechanically "loaded" protein strands. Because of the small size of the crystallites, the internal interfaces in a fiber exceed the external surface by a huge amount, namely, by a factor on the order of $L/D \simeq 10^3$. Mechanical properties, including viscoelasticity, as well as transport properties and the uptake of solvents may be significantly influenced by the properties of these interfaces. Under mechanical load, polypeptides at these interfaces may then transform from the crystalline to an amorphous state, in agreement with the observed size reduction of the crystallites. This interpretation is also supported by the results of hysteresis

measurements,[31] which shows that the envelope of repeated hysteresis cycles forms a normal force−strain curve.[31] This is an indication for irreversible processes in the fiber during stretching, which could also be attributed to an exfoliation of crystallites, as described above.

A further key for the understanding of the mechanical properties could be the variation of properties with relative humidity. The stress−strain curves show a pronounced transition with relative humidity,[31] see Figure 3b. Note that a similar behavior is known for synthetic polyamides, such as Nylon 6.6, which show a similar behavior when wetted.[32] It is plausible that the water diffuses into the amorphous parts of the fibers and replaces hydrogen bonds between the polymer strands, such that the system softens. This transition induced by changes in the amorphous matrix (where water uptake is possible) indicates the importance of the amorphous matrix for the extensibility and the initial elastic modulus, whereas the irreversible changes related to energy dissipation would take place primarily in the crystallites, which at the same time also reinforce the matrix. Investigations of structural changes as a function of both external strain and relative humidity may shed further light on these issues. Finally, it would be important to further characterize the structural properties of the amorphous matrix, which, however, seems difficult due to the predominance of the crystalline components in the scattering intensity distribution.

Acknowledgment. We thank Annette Zippelius and Stefan Ulrich for fruitful discussions, as well as Christian Riekel, Klaus Giewekemeyer and Sebastain Panknin for help at the beamtime. We gratefully acknowledge financial support by the Deutsche Forschungsgemeinschaft (DFG) through Grant SFB602/B6.

References and Notes

(1) Grubb, D. T.; Jelinski, L. W. *Macromolecules* **1997**, *30*, 2860−2867.
(2) Fossey, S. A.; Kaplan, D. L. Silk Protein. In *Polymer Data Handbook*; Oxford University Press: New York, 1999.
(3) Gosline, J. M.; Guerette, P. A.; Ortlepp, C. S.; Savage, K. N. *J. Exp. Biol.* **1999**, *202*, 3295−3303.
(4) Kaplan, D., Ed. *Silk Polymers: Material Science and Biotechnology*; ACS Symposium Series 554; American Chemical Society: Washington, DC, 1994.
(5) Peters, H. M. *Z. Naturforsch.* **1955**, *10b*, 396.
(6) Huemmerich, D.; Scheibel, T.; Vollrath, F.; Cohen, S.; Gat, U.; Ittah, S. *Curr. Biol.* **2004**, *14*, 2070−2074.
(7) Scheibel, T. *Appl. Phys. A* **2006**, *82*, 219−222, 2006.
(8) Puxkandl, R.; Zizak, I.; Paris, O.; Keckes, J.; Tesch, W.; Bernstorff, S.; Purslow, P.; Fratzl, P. *Philos. Trans. R. Soc. London, Ser. B* **2002**, *357*, 191−197.
(9) Roschger, P.; Grabner, B. M.; Rinnerthaler, S.; Tesch, W.; Kneissel, M.; Berzlanovich, A.; Klaushofer, K.; Fratzl, P. *J. Struct. Biol.* **2001**, *136*, 126−136.
(10) Als-Nielsen, J.; McMorrow, D. In *Elements of Modern X-ray Physics*; John Wiley & Sons: New York, 2001; Chapter 4.6.2.
(11) Riekel, C.; Mueller, M.; Vollrath, F. *Macromolecules* **1999**, *32*, 4464−4466.
(12) Riekel, C.; Madsen, B.; Knight, B.; Vollrath, F. *Biomacromolecules* **2000**, *1*, 622−626.
(13) Riekel, C.; Vollrath, F. F. *Int. J. Biol. Macromol.* **2001**, *29*, 203−210.
(14) He, S.-J.; Valluzzi, R.; Gido, S. P. *Int. J. Biol. Macromol.* **1999**, *24*, 187−195.
(15) Riekel, C.; Rössle, M.; Sapede, D.; Vollrath, F. *Naturwissenschaften* **2004**, *91*, 30−33.
(16) Sapede, D.; Seydel, T.; Forsyth, V. T.; Koza, M. M.; Schweins, R.; Vollrath, F.; Riekel, C. C. *Macromolecules* **2005**, *38*, 8447−8453.
(17) Becker, M. Tuross, N. Initial Degradative Changes Found in Bombyx mori Silk Fibroin. In *Silk Polymers: Materials Science and Biotechnology*; Kaplan, D., Adams, W. W., Farmer, B., Viney, C., Eds. ACS Symposium 544; American Chemical Society: Washington, DC, 1994.
(18) Xu, M.; Lewis, R. V. *Proc. Natl. Acad.Sci. U.S.A.* **1990**, *87*, 7120−7124.
(19) Hinman, M. B.; Lewis, R. V. *J. Biol. Chem.* **1992**, *267*, 19320−19324.
(20) Lazzari, M., Liu, G., Lecommandoux, S., Eds. *Block Copolymers in Nanoscience*; Wiley-VCH: Weinheim, Germany, 2007.
(21) Parkhe, A. D.; Seely, S. K.; Gardner, K.; Thompson, L.; Lewis, R. V. *J. Mol. Recognit.* **1997**, *10*, 1−6.
(22) Thiel, B. L.; Guess, K. B.; Viney, C. *Biopolymers* **1997**, *41*, 703−719.
(23) van Beek, J. D.; Hess, S.; Vollrath, F.; Meier, B. H. *Proc. Natl. Acad.Sci. U.S.A.* **2002**, *99*, 10226−10271.
(24) Warwicker, J. O. *J. Mol. Biol.* **1960**, *2*, 350−362.
(25) Marsh, R. E.; Corey, R. B.; Pauling, L. *Biochim. Biophys. Acta* **1955**, *16*, 1−34.
(26) Glišović A.; Salditt, T. *Appl. Phys. A* **2007**, *87*, 63−69.
(27) Glišović, A. *Röntgenstrukturanalyse von Spinnenseiden*, Diplomarbeit, Universität des Saarlandes, 2004.
(28) Work, R. W.; Emerson, P. D. *J. Arachnology* **1982**, *10*, 1−10.
(29) Riekel, C.; Davies, R. J. *Curr. Opin. Colloid Interface Sci.* **2005**, *9*, 369−403.
(30) Kirkpatrick, P.; Baez, A. V. *J. Opt. Soc. Am.* **1948**, *38*, 766−774.
(31) Vehoff, T.; Glišović, A.; Schollmeyer, H.; Salditt, T. *Biophys. J.*, in press.
(32) Michielsen, S. *J. Appl. Polym. Sci.* **1994**, *52*, 1081−1089.
(33) Glisovic, A. Structure Changes in Nephila Dragline: The Influence of Temperature, Humidity and Mechanical Load. Dissertation, Georg-August-Universität Göttingen, 2007.

MA070528P